Smart Structures and Systems, *Vol. 31, No. 5 (2023) 517-529*
https://doi.org/10.12989/sss.2023.31.5.517

An analytical model of the additional confining stress in a prestress-reinforced embankment

Fang Xu [1a], Wuming Leng [1b], Xi Ai [1], Hossein Moayedi [2], Qishu Zhang [1] and Xinyu Ye*[1]

[1] *School of Civil Engineering, Central South University, Changsha 410075, China*
[2] *Institute of Research and Development, Duy Tan University, Da Nang 550000, Vietnam*

(*Received December 12, 2022, Revised March 24, 2023, Accepted March 2023*)

Abstract. Using a device composed of two lateral pressure plates (LPPs) and a steel reinforcement bar to apply horizontal pressure on slope surfaces, a newly developed prestress-reinforced embankment (PRE) is proposed, to which can be adopted in strengthening railway subgrades. In this study, an analytical model, which is available of calculating additional confining stress (σ_H) at any point in a PRE, was established based on the theory of elasticity. In addition, to verify the proposed analytical model, three dimensional (3D) finite element analyses were conducted and the feasibility in application was also identified and discussed. In order to study the performance of the PRE, the propagation of σ_H in a PRE was analyzed and discussed based on the analytical model. For the aim of convenience in application, calculation charts were developed in terms of three dimensionless parameters, and they can be used to accurately and efficiently predict the σ_H in a PRE regardless of the embankment slope ratio and LPP side length ratio. Finally, the potential applications of the proposed analytical model were discussed.

Keywords: additional confining stress; analytical model; calculation chart; embankment; numerical simulation

1. Introduction

Railway transportation is facing increasing challenges with the rapid development of high-speed transportation, heavy-haul freight, and large train densities (Esmaeili and Arbabi 2015, Li 2018, Lazorenko *et al*. 2019, Marjani and Younesian 2019, Kece *et al*. 2019, Sun *et al*. 2019, Wang *et al*. 2020). The increase in axle loads, length, and speed of trains greatly increases vertical dynamic loads, loading cycles, and loading frequency on railways (Tang *et al*. 2016, Xu *et al*. 2018b, Wang *et al*. 2019, Li *et al*. 2020). As a result, the requirements on quality of railway subgrades become increasing strict, and the greater dynamic and frequent loads lead to increasing degradation problems in railways such as large settlement, lateral deformation of embankment shoulder, slope collapse, and degradation of track geometry (Das and Bajpai 2018, Sayeed and Shahin 2018, Khan and Dasaka 2019, Skrypnyk *et al*. 2019, Xu *et al*. 2020).

In this regard, a number of treatment methods, e.g., jet-grouting columns (Lazorenko *et al*. 2019), micro-piles (Dong *et al*. 2018), geogrids (Esmaeili *et al*. 2018), and grouting (Roghani *et al*. 2017), are employed for enhancing railway embankments/subgrades. When implementing the aforementioned methods, the interruption of traffic is needed for the requirement of working space, and they generally need long construction period or lead to environment contamination or result in large disturbance of the embankment. To avoid the problems by using those enhancement methods, Xu *et al*. (2018a) developed a new prestressed reinforcement method and introduced its application in railway embankments; a diagram of a prestress-reinforced embankment (PRE) is shown in Fig. 1. The prestressed reinforcement device is composed of a steel reinforcement bar and two lateral pressure plates (LPPs). The steel bar is protected using a sleeve tube; therefore, there are no contact, friction, and bonding between the steel bar and surrounding soils. Once the steel bar is pulled, it then provides a pre-tension force between the two LPPs, which finally convert that pre-tension force into horizontal pressures acting on the embankment slopes. Therefore, the effect of the reinforcement device is that it can improve the stress state condition in the embankment by applying additional confining stress to the embankment soil, and then improve the performance of the embankment/subgrade (Xu *et al*. 2018a). As the components of the reinforcement device can be prefabricated in manufactory, conveniently assembled and installed in the field, it can reduce economic losses considerably by avoiding traffic interruption and shortening construction period; these merits are important to the normal operation of a railway.

Prestressed reinforcing techniques such as prestressed anchors (Palop *et al*. 2013, Ozhan and Guler 2018), anchored cables (Castro-Fresno *et al*. 2009, Bi *et al*. 2019), anchored bolts (Fahimifar and Ranjbarnia 2009, Wu *et al*. 2019), and anchored cable-frame system (Deng *et al*. 2017, Shi *et al*. 2019) have been widely adopted in stabilizing

*Corresponding author, Ph.D.,
E-mail: yexinyu113@csu.edu.cn
[a] Ph.D., E-mail: fangxu@csu.edu.cn
[b] Ph.D., Professor, E-mail: wmleng@csu.edu.cn

ISSN: 1738-1584 (Print), 1738-1991 (Online)

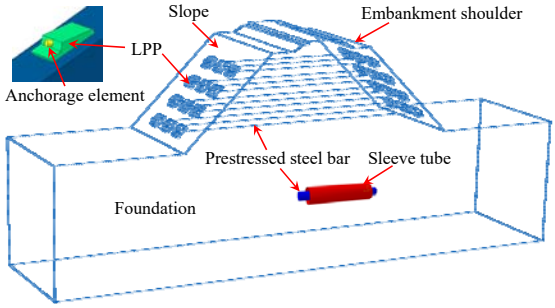

Fig. 1 Schematic diagram of a PRE

slopes, tunnels and deep pit excavations. The efficient and accurate determination of the addition stresses in a prestress-reinforced geotechnical structure is essential for exploring its reinforcement mechanism and potential applications, which plays a decisive role in determining the key design parameters such as the distribution of prestress, required pre-tension force, stability of the PRE, and the required spacing of the LPPs. Analytical methods are more efficient in analyzing the additional stress field in a prestress-reinforced soil/rock mass comparing with numerical methods and laboratory/field tests. Papanastassopoulou-Tsatsanifou (1983) proposed an analytical model to calculate the additional stresses induced by a prestressed rockbolt, in which a pair of line loads was used to simulate the anchoring effects. Wu *et al*. (2010) developed an analytical model for analyzing the stress filed of rock mass by simplifying the anchoring effects of an anchored-bolt as a pair of opposite point loads; similar simplifications were also adopted in the studies of Fahimifar and Ranjbarnia (2009), Guan *et al*. (2007), Carranza-Torres (2009) and Bobet and Einstein (2011). Guo *et al*. (2013) presented analytical solutions to compute the additional stresses surrounding a prestressed rockbolt, in which the anchor plate and anchor bond forces were replaced by using a uniform annular pressure and a point load, respectively. Showkati *et al*. (2015, 2016) proposed an analytical model to calculate the additional stresses subjected to a prestressed anchor while considering the nonlinear distribution of the mobilized interfacial shear stresses around the anchor bonded area. The above analytical methods mostly model the prestressed anchors/rockbolts as point/line loads, which are not in accordance with the reality of a PRE because the LPP loads cannot be simplified as point/line loads. Furthermore, as a newly developed reinforcement technique, the composition and structure of a PRE are different from the existing prestressed reinforcing techniques, therefore the existing analytical models are not applicable for PREs.

Since the stress distribution plays an important role in the performance of the PRE, the study of the propagation of the additional confining stress (σ_H) (i.e., the additional horizontal stress) derived from applying the prestressed reinforcement device is conducted. An analytical model for a PRE was first proposed to calculate the σ_H at any point in a PRE, where the validity and feasibility in application of the model were verified and identified using finite element simulations. The propagation of σ_H in a PRE was then described and discussed based on the analytical model. Finally, calculation charts were developed in terms of three dimensionless parameters for accurately and efficiently predicting the σ_H in a PRE, and the potential applications of the proposed analytical model were finally discussed.

2. Analytical model

2.1 Basic assumptions

An analytical model for calculating the additional stresses in a PRE subjected to the application of the prestressed reinforcement device was developed based on the following assumptions.

(1) The embankment soil matrix is elastic, isotropic, and homogeneous. Soils, in most cases, are not fully elastic, isotropic, or homogeneous materials; however, previous studies have demonstrated that calculations for evaluating additional stresses yield fairly good results for practical work (Das and Sobhan 2014, Budhu 2011, Terzaghi *et al*. 1996).

(2) The pressure between the LPP and the embankment slope is uniform. The distribution of contact pressures between structures and soils is closely related to the magnitude of pressure, the rigidity of the structure, and the modulus of the soil. The LPP is made of reinforced concrete which generally has a rigidity much greater than that of the soil, and it has been proved that simplifying the contact pressure as a uniform loading can yield acceptable predictions of additional stresses in a soil matrix, especially for the regions that are not close to the loading boundary (e.g., the core zones below the rails and sleepers of a PRE) (Das and Sobhan 2014, Budhu 2011, Terzaghi *et al*. 1996).

(3) There is no interaction between the steel bar and embankment soil. The steel reinforcement bar is separated from the embankment soil using a sleeve protection tube as presented in Fig. 1; therefore, the interaction between the steel bar and embankment soil is negligible.

2.2 Solutions for additional stress components

Fig. 2 is a schematic diagram of the analytical model for a PRE, where the *x*-, *y*-, and *z*-axes parallel to the embankment slope, the longitudinal direction, and the direction perpendicular to the slope surface, respectively. The LPP transforms the pre-tension force (F) of the steel reinforcement bar into an equivalent horizontal pressure (q) acting on the embankment slope; q can be further decomposed into a uniform normal pressure (q_N) and a uniform tangential pressure (q_T), as shown in Fig. 2. The side lengths of the LPP in the x and y directions and the embankment slope angle are identified as w, l, and θ in Fig. 2, respectively. Using these variables, q, q_N, and q_T can then be calculated using Eqs. (1)-(3) as shown below.

$$q = \frac{F}{wl} \tag{1}$$

$$q_T = q\cos\theta \tag{2}$$

$$q_T = q\sin\theta \tag{3}$$

The normal and tangential loads applied on an arbitrary microelement loading area ($dA = dxdy$) of the LPP can be expressed as $dN = q_N dxdy$ and $dT = q_T dxdy$, respectively. When dA is concentrated to a point, dN and dT can be regarded as point loads; then the components of the additional stress below a corner point of an LPP under the action of q_N and q_T can be calculated by integrating the solutions of Boussinesq (1885) and Cerruti (1882). The detailed expressions of the derived stress components are Eqs. (4)-(9), where compression normal stresses and shear stresses that counterclockwise around the LPP are positive (+). Specifically, the result using Eq. (6) is positive when the calculation point is below the lower corner points of the LPP, and the results are also positive using Eqs. (7) and (8) when the calculation point is below the upper corner points of the LPP, and vice versa.

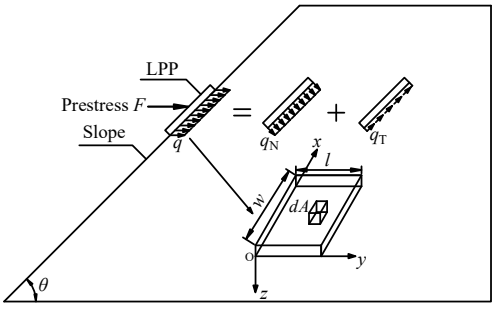

Fig. 2 Schematic diagram of the analytical model for a PRE

2.3 Calculation of the additional confining stress

Based on the stress state analysis theory, the additional confining stress (σ_H) in the horizontal direction can be formulated as

$$\sigma_H = r^2\sigma_x + n^2\sigma_z + 2nr\tau_{zx} \tag{10}$$

$$\sigma_{zN} = \iint_S \frac{3q_N z^3}{2\pi R^5}dxdy = \frac{q_N}{2\pi}\left[\frac{wlz(w^2+l^2+2z^2)}{(w^2+z^2)(l^2+z^2)\sqrt{w^2+l^2+z^2}} + arctan\left(\frac{wl}{z\sqrt{w^2+l^2+z^2}}\right)\right] \tag{4}$$

$$\begin{aligned}\sigma_{xN} = \iint_S \frac{3q_N}{2\pi}\left[\frac{x^2 z}{R^5} + \frac{1-2\mu}{3}\left(\frac{1}{R(R+z)} - \frac{(2R+z)y^2}{R^3(R+z)^2} - \frac{z}{R^3}\right)\right]dxdy = \frac{q_N}{2\pi}(2\mu-1)\arctan\left(\frac{wl}{z\sqrt{w^2+l^2+z^2}}\right)\\ + \frac{q_N}{2\pi}\left[-\frac{wlz}{(w^2+z^2)\sqrt{w^2+l^2+z^2}} + \arctan\left(\frac{wl}{z\sqrt{w^2+l^2+z^2}}\right)\right]\\ - \frac{q_N(2\mu-1)}{2\pi}\left[\arctan\left(\frac{l}{w}\right) - \arctan\left(\frac{lz}{w\sqrt{w^2+l^2+z^2}}\right)\right]\end{aligned} \tag{5}$$

$$\tau_{xzN} = \pm\iint_S \frac{3q_N xz^2}{2\pi R^5}dxdy = \pm\frac{q_N z^2}{2\pi}\left[\frac{l}{z^2\sqrt{l^2+z^2}} - \frac{l}{(w^2+z^2)\sqrt{w^2+l^2+z^2}}\right] \tag{6}$$

$$\sigma_{zT} = \pm\iint_S \frac{3q_T xz^2}{2\pi R^5}dxdy = \pm\frac{q_T z^2}{2\pi}\left[\frac{l}{z^2\sqrt{l^2+z^2}} - \frac{l}{(w^2+z^2)\sqrt{w^2+l^2+z^2}}\right] \tag{7}$$

$$\begin{aligned}\sigma_{xT} &= \pm\iint_S \frac{q_T x}{2\pi R^3}\left[\frac{1-2\mu}{(R+z)^2}\left(R^2 - y^2 - \frac{2Ry^2}{R+z}\right) - \frac{3x^2}{R^2}\right]dxdy\\ &= \pm\left\{\begin{array}{l}\dfrac{q_T(1-2\mu)}{2\pi l(w^2+l^2)}\left[w^2\left(-z+\sqrt{l^2+z^2}\right) + l^2\left(\sqrt{l^2+z^2} - \sqrt{w^2+l^2+z^2}\right)\right]\\ + \dfrac{q_T}{2\pi}\left[\dfrac{w^2 l}{(w^2+z^2)\sqrt{w^2+l^2+z^2}} + ln\left(1 - \dfrac{l}{\sqrt{l^2+z^2}}\right) - ln\left(1 + \dfrac{l}{\sqrt{l^2+z^2}}\right)\right.\\ \left.+2\,ln\left(l+\sqrt{w^2+l^2+z^2}\right) - 2\,ln\left(\sqrt{w^2+z^2}\right)\right]\end{array}\right\}\end{aligned} \tag{8}$$

$$\tau_{xzT} = \iint_S \frac{3q_T x^2 z}{2\pi R^5}dxdy = \frac{q_T}{2\pi}\left[-\frac{wlz}{(w^2+z^2)\sqrt{w^2+l^2+z^2}} + \arctan\left(\frac{wl}{z\sqrt{w^2+l^2+z^2}}\right)\right] \tag{9}$$

where $R = (x^2 + y^2 + z^2)^{1/2}$ is the distance between the calculation point P and the coordinate origin O (see Fig. 2); μ is Poisson's ratio; σ_{xN}, σ_{zN}, and τ_{xzN} are additional stresses along the x and z directions and the shear stress in the xz plane subjected to q_N, respectively; and σ_{xT}, σ_{zT}, and τ_{xzT} are the corresponding additional stress components subjected to q_T.

where σ_x, σ_z, and τ_{xz} are the additional stresses along the x and z directions and the shear stress in the xz plane subjected to q; r (= cos(H, x) = cosθ) and n (= cos(H, z) = sinθ) are direction cosines.

As σ_{xN} and σ_{zN} are symmetrically distributed and τ_{xzN} is anti-symmetrically distributed under the action of q_N, and σ_{xN} and σ_{zN} are anti-symmetrically distributed and τ_{xzN} is symmetrically distributed under the action of q_T, the

additional confining stresses (σ_{HU} and σ_{HD}) at a distance z (in the z direction) from the upper and lower corner points of an LPP can be calculated using Eqs. (11) and (12).

$$\sigma_{\mathrm{HU}} = qK_{zU} = (\sigma_{xN} + \sigma_{xT})\cos^2\theta + (\sigma_{xN} + \sigma_{xT})\sin^2\theta + (-|\tau_{xzN}| + \tau_{\mathrm{xzT}})\sin 2\theta \tag{11}$$

$$\sigma_{\mathrm{HD}} = qK_{zD} = (\sigma_{xN} - |\sigma_{xT}|)\cos^2\theta + (\sigma_{zN} - |\sigma_{zT}|)\sin^2\theta + (\tau_{xzN} + \tau_{xzT})\sin 2\theta \tag{12}$$

where $K_{z\mathrm{U}}$ and $K_{z\mathrm{D}}$ are coefficients of additional confining stress at a distance z (along the z direction) from the upper and lower corner points of an LPP, respectively. The detailed expressions for $K_{z\mathrm{U}}$ and $K_{z\mathrm{D}}$ are Eqs. (13) and (14).

$$\begin{aligned}
K_{zU} = {} & \left\{\left\{\frac{q(2\mu-1)}{2\pi}\arctan\left(\frac{wl}{z\sqrt{w^2+l^2+z^2}}\right) + \frac{q}{2\pi}\left[-\frac{wlz}{(w^2+z^2)\sqrt{w^2+l^2+z^2}} + \arctan\left(\frac{wl}{z\sqrt{w^2+l^2+z^2}}\right)\right]\right.\right. \\
& \left.\left. -\frac{q(2\mu-1)}{2\pi}\left[\arctan\left(\frac{l}{w}\right) - \arctan\left(\frac{lz}{w\sqrt{w^2+l^2+z^2}}\right)\right]\right\}\sin\theta \right. \\
& -\left\{\frac{q(1-2\mu)\left[w^2\left(-z+\sqrt{l^2+z^2}\right)+l^2\left(\sqrt{l^2+z^2}-\sqrt{w^2+l^2+z^2}\right)\right]}{2l(w^2+l^2)\pi} + \frac{q}{2\pi}\left[\frac{w^2 l}{(w^2+z^2)\sqrt{w^2+l^2+z^2}}\right.\right. \\
& \left.\left. -2\ln\left(\sqrt{w^2+z^2}\right) + \ln\left(1-\frac{l}{\sqrt{l^2+z^2}}\right) - \ln\left(1+\frac{l}{\sqrt{l^2+z^2}}\right) + 2\ln\left(l+\sqrt{w^2+l^2+z^2}\right)\right]\right\}\cos\theta\Big\}\cos^2\theta \\
& +\left\{\frac{q}{2\pi}\left[\frac{wlz(w^2+l^2+2z^2)}{(w^2+z^2)(l^2+z^2)\sqrt{w^2+l^2+z^2}} + \arctan\left(\frac{wl}{z\sqrt{w^2+l^2+z^2}}\right)\right]\sin\theta\right. \\
& \left.-\frac{qz^2}{2\pi}\left[-\frac{l}{z^2\sqrt{l^2+z^2}} + \frac{l}{(w^2+z^2)\sqrt{w^2+l^2+z^2}}\right]\cos\theta\right\}\sin^2\theta \\
& -\left\{-\frac{qz^2}{2\pi}\left[\frac{l}{z^2\sqrt{l^2+z^2}} - \frac{l}{(w^2+z^2)\sqrt{w^2+l^2+z^2}}\right]\sin\theta\right. \\
& \left.+\frac{q}{2\pi}\left[\frac{wlz}{(w^2+z^2)\sqrt{w^2+l^2+z^2}} - \arctan\left(\frac{wl}{z\sqrt{w^2+l^2+z^2}}\right)\right]\cos\theta\right\}\sin 2\theta
\end{aligned} \tag{13}$$

$$\begin{aligned}
K_{zD} = {} & \left\{\left\{\frac{q(2\mu-1)}{2\pi}\arctan\left(\frac{wl}{z\sqrt{w^2+l^2+z^2}}\right) + \frac{q}{2\pi}\left[-\frac{wlz}{(w^2+z^2)\sqrt{w^2+l^2+z^2}} + \arctan\left(\frac{wl}{z\sqrt{w^2+l^2+z^2}}\right)\right]\right.\right. \\
& \left.\left. -\frac{q(2\mu-1)}{2\pi}\left[\arctan\left(\frac{l}{w}\right) - \arctan\left(\frac{lz}{w\sqrt{w^2+l^2+z^2}}\right)\right]\right\}\cos\theta \right. \\
& +\left\{\frac{q(1-2\mu)\left[w^2\left(-z+\sqrt{l^2+z^2}\right)+l^2\left(\sqrt{l^2+z^2}-\sqrt{w^2+l^2+z^2}\right)\right]}{2l(w^2+l^2)\pi}\right. \\
& +\frac{q}{2\pi}\left[\frac{w^2 l}{(w^2+z^2)\sqrt{w^2+l^2+z^2}} - 2\ln\left(\sqrt{w^2+z^2}\right) + \ln\left(1-\frac{l}{\sqrt{l^2+z^2}}\right) - \ln\left(1+\frac{l}{\sqrt{l^2+z^2}}\right)\right. \\
& \left.\left.+2\ln\left(l+\sqrt{w^2+l^2+z^2}\right)\right]\right\}\cos\theta\Big\}\cos^2\theta \\
& +\left\{\frac{q}{2\pi}\left[\frac{wlz(w^2+l^2+2z^2)}{(w^2+z^2)(l^2+z^2)\sqrt{w^2+l^2+z^2}} + \arctan\left(\frac{wl}{z\sqrt{w^2+l^2+z^2}}\right)\right]\sin\theta\right. \\
& \left.+\frac{qz^2}{2\pi}\left(-\frac{l}{z^2\sqrt{l^2+z^2}} + \frac{l}{(w^2+z^2)\sqrt{w^2+l^2+z^2}}\right)\cos\theta\right\}\sin^2\theta \\
& -\left\{\frac{qz^2}{2\pi}\left[\frac{l}{z^2\sqrt{l^2+z^2}} - \frac{l}{(w^2+z^2)\sqrt{w^2+l^2+z^2}}\right]\cos\left(\frac{\pi}{2}-\theta\right)\right. \\
& \left.+\frac{q}{2\pi}\left[\frac{wlz}{(w^2+z^2)\sqrt{w^2+l^2+z^2}} - \arctan\left(\frac{wl}{z\sqrt{w^2+l^2+z^2}}\right)\right]\cos\theta\right\}\sin 2\theta
\end{aligned} \tag{14}$$

The additional confining stress on the horizontal path H behind the upper corner point C can be calculated using the block method, as shown in Fig. 3. The variable h denotes the horizontal distance of a calculation point to the slope surface along the horizontal path H; point D is the projection of P on the embankment slope. The side lengths of subdivided loading regions DOAE and DCBE along the x direction are (w + $h$cosθ) and $h$cosθ, respectively, and the calculation depth in the z direction is $h$sinθ. The additional confining stress (σ_{HU}) on the horizontal path H behind the upper corner point C is calculated as the superimposed confining stress imposed by loading regions DOAE and DCBE, and the equation is

$$\begin{aligned}
\sigma_{\mathrm{HU}} &= qK_{\mathrm{HU}} = \sigma_{\text{HU-DOAE}} - \sigma_{\text{HU-DCBE}} \\
&= q(K_{\text{zU-DOAE}} - K_{\text{zU-DCBE}})
\end{aligned} \tag{15}$$

where K_{HU} is the coefficient of additional confining stress on the horizontal path H behind the upper corner point C; the subscripts of DOAE and DCBE correspond to the

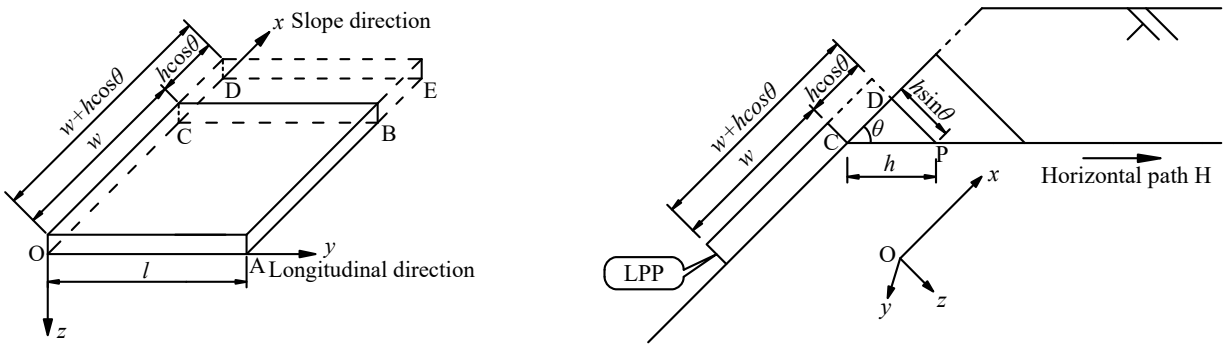

(a) Subdivided regions of the LPP (b) Conversion of the calculation path

Fig. 3 Schematic diagram for calculating σHU or KHU behind an upper corner of the LPP

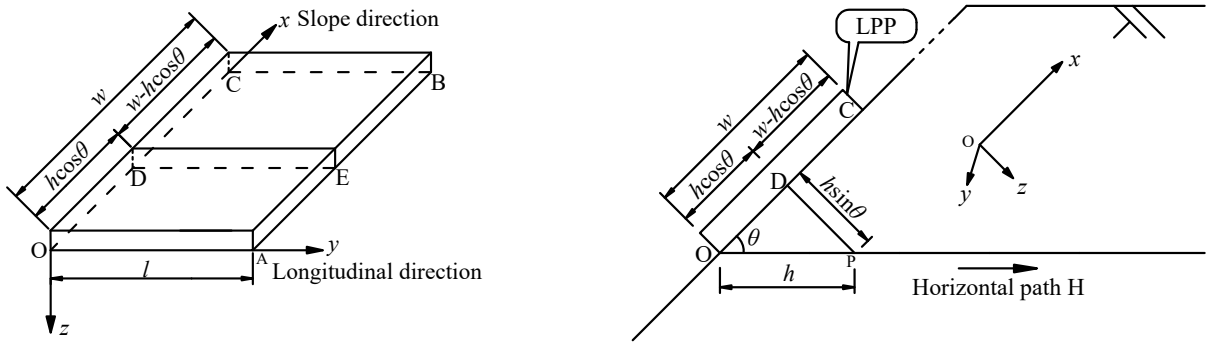

(a) Subdivided regions of the LPP (b) Conversion of the calculation path

Fig. 4 Schematic diagram for calculating σHD or KHD behind a lower corner of the LPP

loading regions.

A procedure similar to the one used to calculate σ_{HU} is used for the additional confining stress (σ_{HD}) on the horizontal path behind the lower corner point O. The σ_{HD} can be calculated as the superimposed confining stress imposed by loading regions DOAE and DEBC, as shown in Fig. 4, where the side lengths of loaded region DEBC along the x direction is ($w - h\cos\theta$) and the calculation depth in the z direction is $h\sin\theta$. The equation for σ_{HD} is

$$\begin{aligned}\sigma_{\mathrm{HD}} = qK_{\mathrm{HD}} &= \sigma_{\mathrm{HU\text{-}DOAE}} + \sigma_{\mathrm{HD\text{-}DEBC}} \\ &= q(K_{z\mathrm{U\text{-}DOAE}} + K_{z\mathrm{D\text{-}DEBC}})\end{aligned} \tag{16}$$

where K_{HD} is the coefficient of additional confining stress on the horizontal path H behind the lower corner point O.

Eqs. (15) and (16) convert the calculation path from the z direction to the H direction, which enables the direct computation of σ_{H} behind an LPP corner point along the horizontal path H and can intuitively reflect the distribution of σ_{H} in a PRE. Eqs (15) and (16) can be abbreviated as

$$\sigma_H = qK_H \tag{17}$$

where K_{H} is the coefficient of additional confining stress described by Eqs. (15) and (16), and the value of K_{H} is determined by w, l, and h (as shown in Figs. 3 and 4).

The block method can also be used to calculate σ_{H} at points that are not on horizontal paths behind the LPP corner points, by dividing the loading area of the LPP into a few rectangular loading regions with the point as a common corner. The σ_{H} at an arbitrary horizontal distance can then be calculated as the superimposed confining stress imposed by the subdivided loading regions. The solutions published by Boussinesq (1885) and Cerruti (1882) were derived on the basis of an elastic semi-infinite space. Previous studies (Lv and Wang 2004, Chen *et al*. 2014) and multinational design codes (German Railway Standard Rail 836 2008, National Railway Administration of the People's Republic of China 2014) have demonstrated that analytical solutions based on semi-infinite space can predict the additional stress in a soil embankment with satisfactory accuracy when the net spacing between the loading boundary and the embankment boundary (e.g., the embankment shoulder line) reaches a certain value. The initial stress field around the embankment shoulder approximates a zero-stress state, hence local shear failure readily occurs when the prestress is applied close to the embankment shoulder line. Therefore, the prestressed reinforcement devices are normally not applied near this line, which is in accordance with the net spacing requirement between the reinforcement devices and embankment shoulder when using the proposed analytical model. However, there is a requirement to identify the required net spacing value to demonstrate the validity and feasibility in application of the proposed model, which is specifically discussed in the next section by comparing with numerical simulations.

3. Numerical verification

3.1 Finite element model

The PRE was analyzed using the ABAQUS software (Dassault Systèmes Simulia Corp., Version 6.14). The embankment has a height of 7.0 m, a half width of 4.15 m, a slope ratio of 1:1, and a length of 15.0 m. The bottom boundary is 15.0 m below the top surface of embankment and the left boundary is 10.0 m away from the embankment toe as presented in Fig. 5, where s denotes the net spacing between the LPP and the embankment shoulder line. The LPP has a plan dimension of 1.0 m × 1.0 m. In the three-dimensional (3D) finite element analyses (FEA), cases with s values of one and two times of the LPP width (i.e., 1 m and 2 m) were simulated to determine which placement was more appropriate.

The adopted soil properties are E = 120 MPa and μ = 0.30 which are within the value ranges of 80-250 MPa and 0.25-0.32 for an embankment filler reported by Gong and Zhou (2007) and Mei *et al*. (2019), where E is Young's modulus and μ is Poisson's ratio. It is worth noting that the absolute values of the involved soil parameters may have an impact on the embankment deformation, but the effect on the distributions of the additional confining stress is limited when the E and μ are within the aforementioned value ranges. The left, right, front, and back boundaries are fixed but vertical displacement is allowed. At the bottom of the model, both vertical and horizontal displacements are fixed. Because the PRE are symmetrical, only one-half of the embankment was analyzed. Fig. 5 shows the established finite element model where 238, 464 reduced integrated hexahedral elements (C3D8R) are generated to mesh the embankment. To ensure the accuracy of the simulations, the mesh in the local regions around the loading area has a smaller size. The applied horizontal pressure (p) was 100 kPa. It should be noted that the degradation of the embankment due to the additional uplift stress may occur once too much pressure is applied on the embankment, so the condition that once the soils under the center of the LPP reach the failure point is identified as the critical state. It is found that the soil under the LPP does not appear a shear failure when the additional stress is under 150 kPa (Wang 2019).

3.2 Validation of the analytical model

The K_H versus h curves at different external distances (d_U, see Fig. 5) from the upper border of the LPP are compared with that using the analytical model, as shown in Figs. 6 and 7. The K_H in the FEAs is calculated as $K_H = S_{11}/p$, where S_{11} is the additional confining stress, and the K_H in the analytical model is evaluated using the superimposed confining stress imposed by a pair of LPPs that are on opposite slopes of the PRE. As shown in Fig. 6, the difference of the K_H versus h curves between the FEAs and analytical curves is large when the net spacing is one time of the LPP width (i.e., 1.0 m). However, this difference is quite small when the net spacing is two times of the LPP width (i.e., 2.0 m) (see Fig. 7), indicating that a net spacing of 2.0 m is sufficient to satisfactorily predict the additional confining stress in the PRE. In addition, the reason that there are some differences between the FEAs and analytical curves may account for the following reason: the soil stress redistribution is occurred for the soil with an elastic-plastic behavior in numerical model, this phenomenon is more obvious for the position that closer to the slope surface of the embankment (e.g., the h is smaller than 0.4 m). The soil in the analytical model is assumed to be elastic matrix, so the difference appears. Nevertheless, as a preliminary guidance, the proposed analytical model is appropriate for analyzing the additional stress field in a PRE when the net spacing is greater than two times of the LPP width (i.e., 2 m in this study). Compared with the finite element method, the proposed analytical model has advantages of strong reliability, high computational efficiency, clear in concept, simple in operation, and ease for engineers to use.

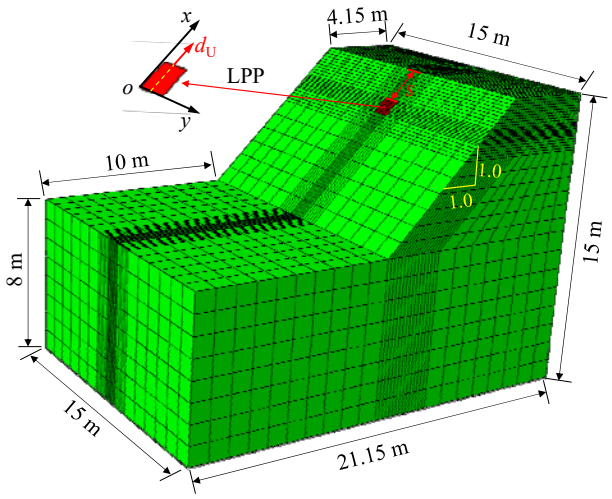

Fig. 5 Numerical model of the PRE

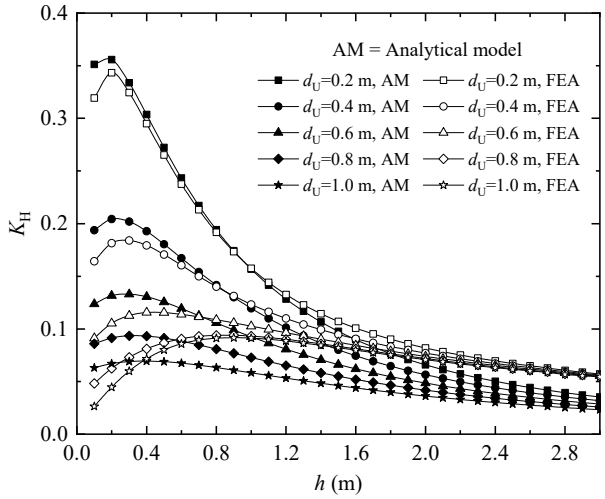

Fig. 6 K_H–h curves outside the LPP for s = 1 m

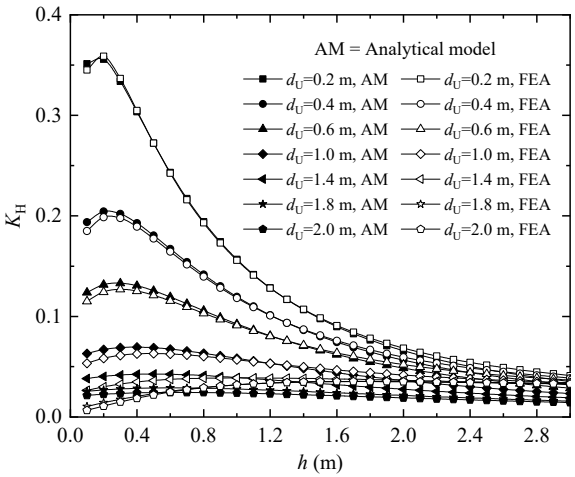

Fig. 7 K_H–h curves outside the LPP for s = 2 m

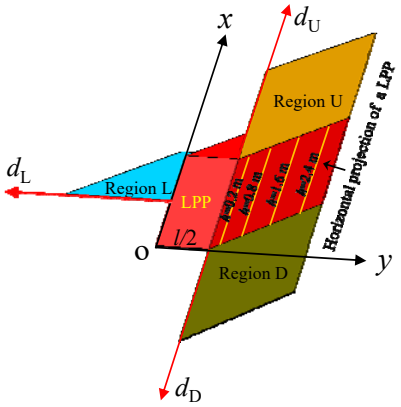

Fig. 8 Diagram showing the positions of analyzed regions in the PRE

4. Distribution of the additional confining stress

Tentative calculations show that the distribution pattern of σ_H in a PRE is similar under different LPP sizes and embankment slope ratios. In this study, the σ_H distribution subjected to single LPP is discussed with a 1.0 m × 1.0 m LPP and a 1:1 embankment slope ratio by using the proposed analytical model and the Mathematica software (Wolfram Research, Inc., version 11.3).

4.1 Additional confining stress behind the LPP

The additional confining stress on four inclined planes, which are 0.2 m, 0.8 m, 1.6 m, and 2.4 m from the LPP (see Fig. 8), are analyzed. Fig. 9 shows 3D color contours of the K_H (or σ_H) on the four projected inclined planes. The contours show that K_H is attenuated with increasing h.

On the nearest plane to the LPP (Fig. 9(a)), the additional confining stress near the lower border is low because the tangential pressure q_T results in tension stress near the LPP's lower border and this tension partially offsets the compression stress induced by the normal pressure q_N. Overall, the K_H contours exhibits a "bulging abdomen" shape on close planes; however, K_H gradually decreases and displays in a much more uniform distribution pattern ("flat abdomen"), as shown in Fig. 9(d). The arrow lines in Fig. 9 indicate the traces of K_H growth; the high stress region moves gradually from the upper part to the lower border of the loading area as h increases. The variation ranges of the K_H are 0.185–1.170, 0.196–0.503, 0.094–0.197, and 0.053–0.095 for the h values of 0.2 m, 0.8 m, 1.6 m, and 2.4 m, respectively. The maximum and minimum values in the shallow regions exhibit a difference of an order of magnitude. However, the difference in K_H then minimized and gradually become uniformly distributed with increasing h.

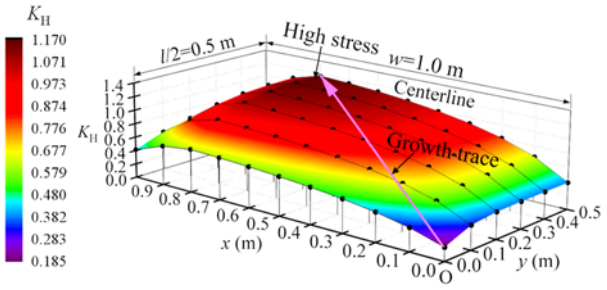

(a) h = 0.2 m

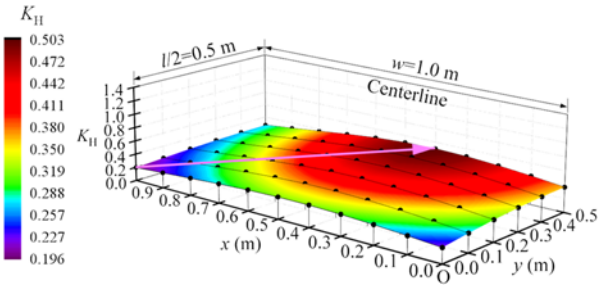

(b) h = 0.8 m

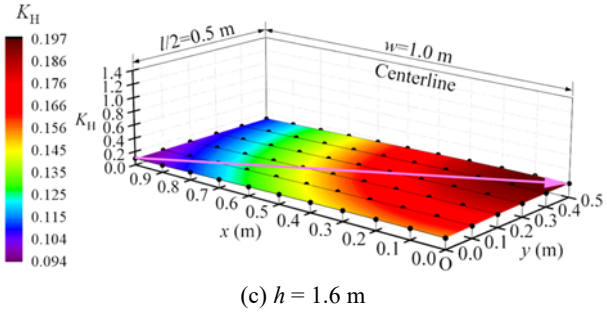

(c) h = 1.6 m

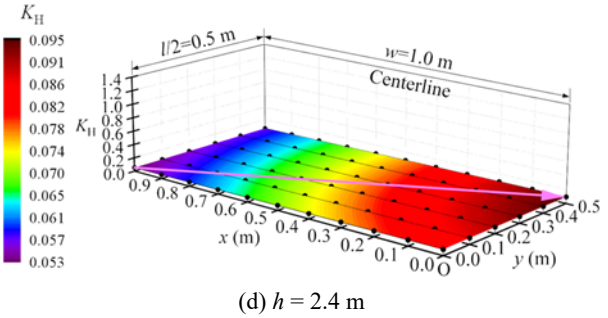

(d) h = 2.4 m

Fig. 9 Distribution contours of K_H on the four inclined planes at different h values

4.2 Additional confining stress in regions adjacent to the LPP

The additional confining stress in a PRE is continuously propagated to the regions beyond the LPPs. The propagation of σ_H to the external regions on the symmetry planes of the LPP, that are regions U, D, and L in Fig. 8, are analyzed in detail, where d_U, d_D, and d_L are the external distance away from the LPP border in regions U, D, and L, respectively (see Fig. 8).

The K_H versus h curves at various external distances (d_U) for region U are shown in Fig. 10. K_H first increases to a maximum value followed by a gradually decrease with increasing h, with each curves showing a peak point. The distance h from the peak stress point to the slope surface increases with increasing d_U, indicating that the prestress gradually expands outward with increasing h. Note that the K_H versus h curves tend to become nearly horizontal when h is greater than 2.4 m, implying that a continuous and effectively reinforced zone can be formed if the pre-tension force and LPP spacing are properly designed.

Fig. 11 shows K_H versus h curves for different external distances (d_L) in region L; there is a peak point on each curve and the K_H expansion is similar to that in region U.

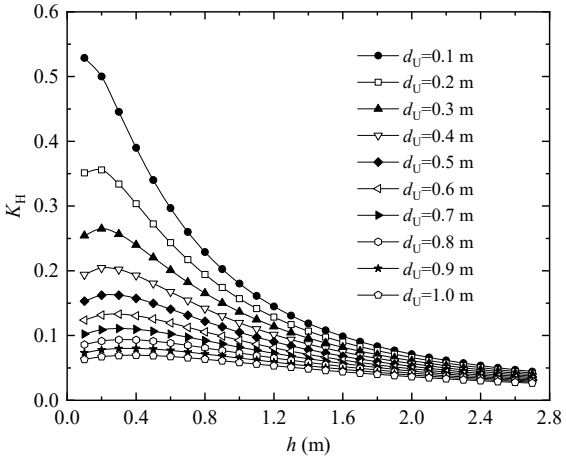

Fig. 10 K_H–h curves in region U

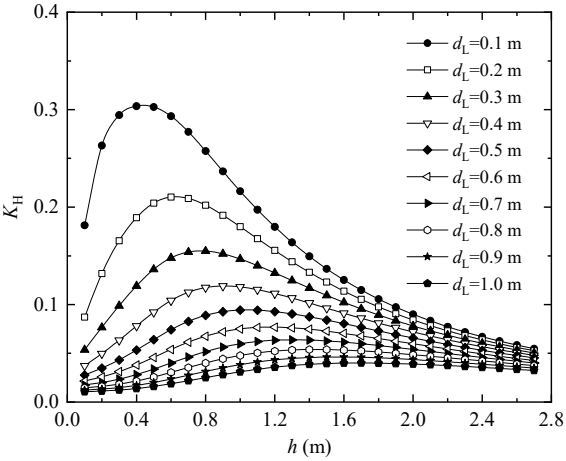

Fig. 11 K_H–h curves in region L

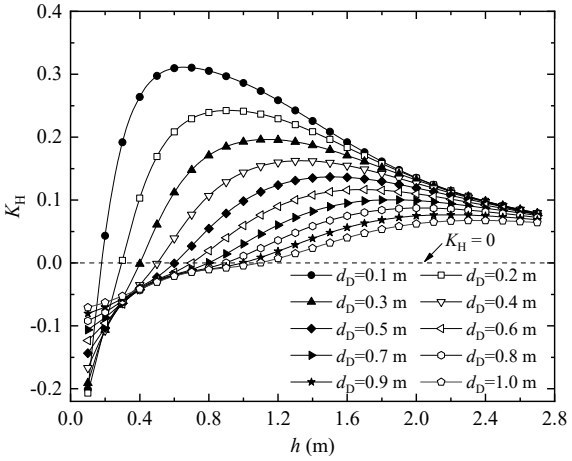

Fig. 12 K_H–h curves in region D

Fig. 12 presents the K_H versus h curves at different external distances (d_D) in region D, showing a peak point on each curve. The curves intersect the horizontal line of K_H = 0, defining a critical distance (h_c) where the additional confining stress changes from tension (–) to compression (+). Theoretically, the magnitude of tension stress and the size of tension region is capable to be offset to a low level by the compression effect of the LPP blow the lower border of the current LPP if the LPP spacing is properly designed. In addition, the K_H versus h curves (Fig. 12) tend to be horizontal when h is greater than 2.4 m, indicating that an effective reinforced zone similar to the one in region U can also be formed in region D.

5. Calculation charts for K_H

The above sections proposed an analytical model for calculating the additional confining stress in a PRE. However, the calculation process is complicated and would be inconvenient in engineering practice. Therefore, calculation charts were developed to enable the efficient prediction of σ_H in practical work. The charts use three dimensionless parameters, namely the embankment slope ratio (1:m), side length ratio of the LPP (l/w), and the ratio (h/w) of h to the width (w) of the LPP along the embankment slope direction. In particular, the coefficients of the additional confining stress (K_{HU} and K_{HD}) under six typical embankment slope ratios (i.e., 1:m = 1:0.50, 1:0.75, 1:1.00, 1:1.25, 1:1.5, and 1:1.75) are calculated using Eqs. (1)-(16), and the calculation charts are presented in Figs. 13 and 14.

5.1 Charts for K_{HU}

Fig. 13 presents K_{HU} versus h/w curves for the six embankment slope ratios, with lines corresponding to different l/w values. The shapes of the K_{HU} versus h/w curves for different slope ratios are similar, that is K_{HU} increases with decreasing slope ratio. Moreover, K_{HU} increases with increasing l/w and the convergence of those curves indicates that the increase rate gradually decreases.

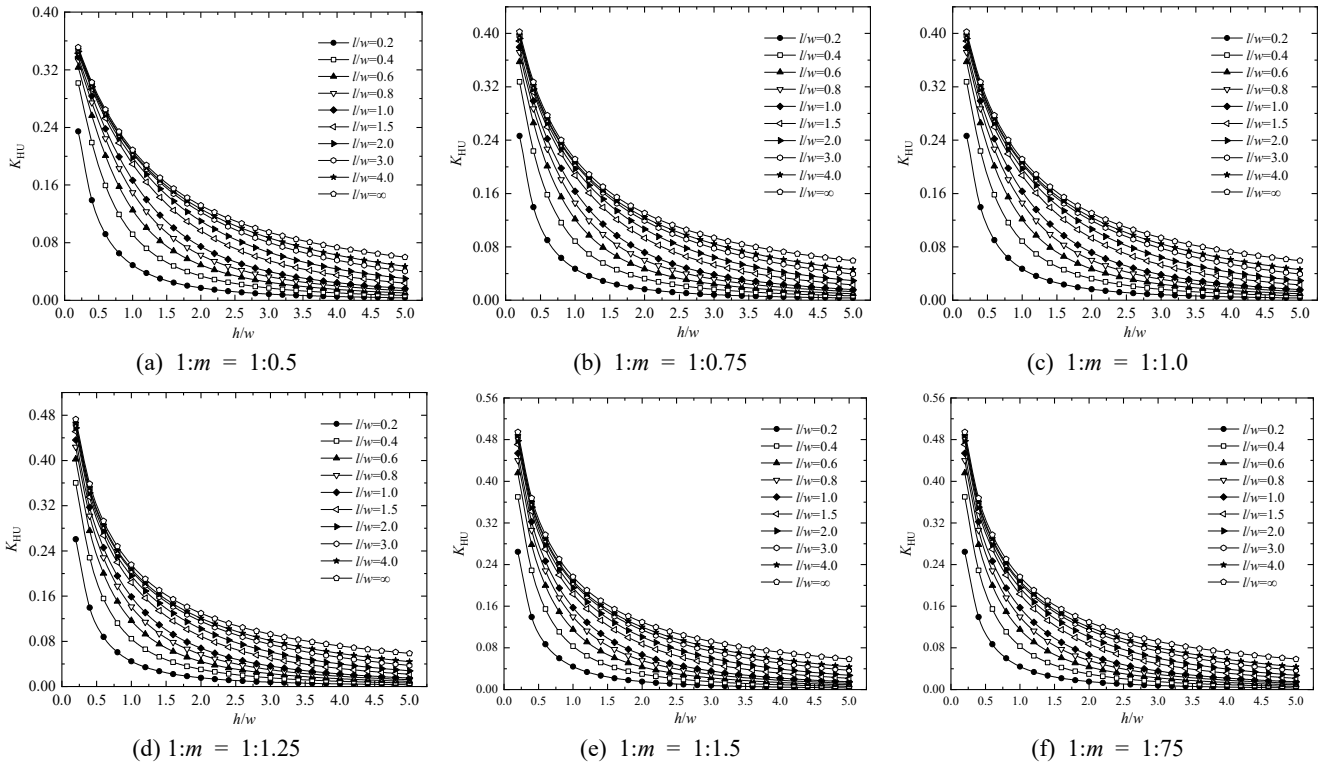

(a) 1:m = 1:0.5 (b) 1:m = 1:0.75 (c) 1:m = 1:1.0

(d) 1:m = 1:1.25 (e) 1:m = 1:1.5 (f) 1:m = 1:75

Fig. 13 K_{HU}–h/w curves for six different PRE slope ratios

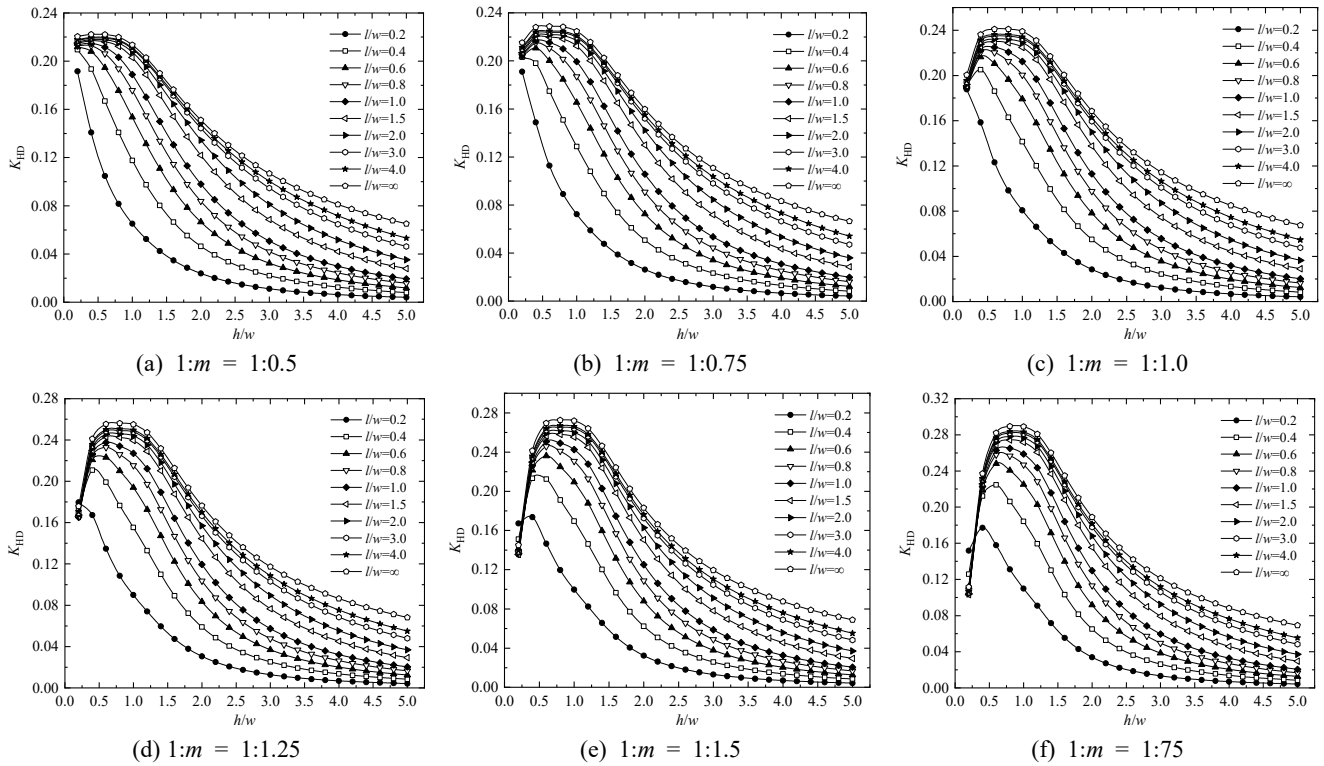

(a) 1:m = 1:0.5 (b) 1:m = 1:0.75 (c) 1:m = 1:1.0

(d) 1:m = 1:1.25 (e) 1:m = 1:1.5 (f) 1:m = 1:75

Fig. 14 K_{HD}–h/w curves for six different PRE slope ratios

5.2 Charts for K_{HD}

Fig. 14 presents K_{HD} versus h/w curves for the six embankment slope ratios. The shapes of the K_{HD} versus h/w curves for different slope ratios are similar. However, there is a critical side length ratio ($(l/w)_c$) for K_{HD} below which K_{HD} decreases with increasing h/w. When l/w is greater than $(l/w)_c$, K_{HD} initially increases to a peak value and then gradually decreases with increasing h/w, with each curve having a peak K_{HD}. Similar to K_{HU}, K_{HD} increases with

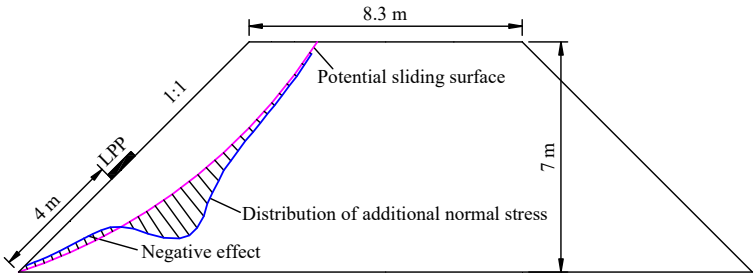

(a) Additional normal stress

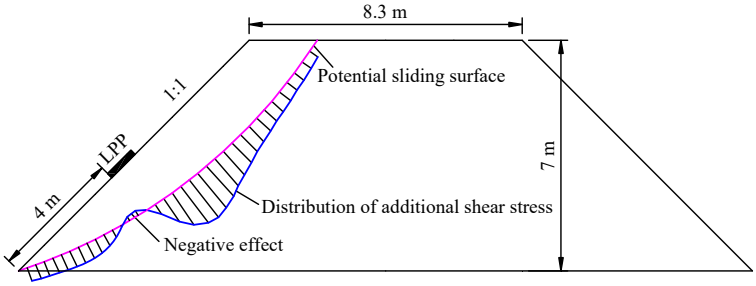

(b) Additional shear stress

Fig. 15 Additional stresses on a potentail sliding surface of a PRE

increasing l/w and the increase rate gradually decreases. It is noted that the curves for K_{HD} (and K_{HU}) versus h/w do not change significantly when l/w is greater 4.0, implying that LPPs should not be designed as a narrow strip. Consequently, the side length ratio (l/w) of the LPP is suggested to be greater than the critical value $(l/w)_c$ but less than 4.0.

The additional confining stress at any point in a PRE can be conveniently obtained using the calculation charts. The procedures and remarks in the prediction of σ_H in a PRE are as follows: (1) calculate the values of l/w and h/w based on the designed LPP dimensions and the position/coordinate of the targeted calculation point; (2) predict the σ_H using l/w, h/w, and Fig. 13 or 14; (3) for cases where the slope ratio, LPP size, and the calculation position are not included in the charts, the interpolation method is suggested; (4) for the situations where σ_H is provided by multiple LPPs, total σ_H can be estimated by using the superposition principle.

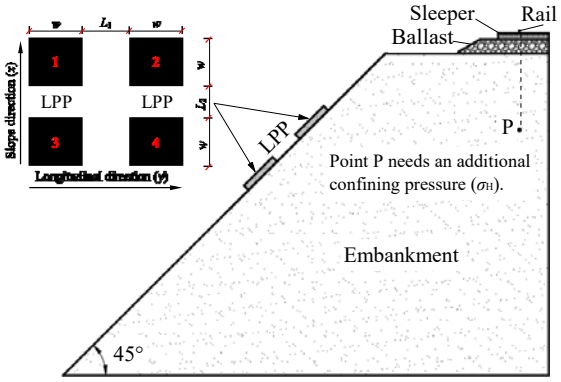

Fig. 16 Schematic diagram of LPP spacing to attain required σ_H

6. Potential applications of the analytical model

The efficient and accurate determination of the addition stresses in a PRE is essential for studying its reinforcement mechanism and potential applications, which plays a decisive role in determining the stability of the PRE, the required spacing of the LPPs, and the required pre-tension force of the steel bar. Fig. 15 presents the distributions of additional normal and shear stresses on a potential sliding surface of the analyzed embankment in section 3 using the developed analytical model, where one row of LPPs (i.e., corresponding to a plain strain condition) is placed with a net spacing of 4 m away from the embankment toe.

The additional normal and shear stresses on the potential sliding surface are calculated based on the proposed analytical model and stress state analysis theory. It can be seen that the additional stresses, predicted using the proposed model, continuously propagate to the entire sliding surface. Tension normal stress appears on the slices beyond the lower boundary of the LPP, resulting in negative effect on the stability of the PRE; however, the tension stress is much less compared with the compression stress. Similarly, the positive effect of the shear stress on the sliding surface is also much greater than the negative effect. Therefore, the stability improvement of the PRE is dominated by the positive effect of the additional normal and shear stresses, and the proposed analytical model could provide a theoretical base to develop a method for analyzing the stability of a PRE by incorporating the propagation effect of additional stresses in future studies.

In recent decades, the increase in axle loads, length, and speed of trains leads to increasing degradation problems in railways such as large settlement, lateral deformation of embankment shoulder, slope collapse, and degradation of

track geometry. It has been proved that increasing the confining pressure of the embankment soil can effectively mitigate the degradation problems of the railway subgrade (Xu *et al*. 2018a). Therefore, how to design the LPP spacing to attain the required confining pressure of the embankment soil is worth of studying.

The increase in axle loads of operation trains may lead to the induced dynamic stress becomes greater than the critical dynamic stress (σ_{cri}) of the embankment soil, thus resulting in excessive plastic deformation of the railway subgrade (Zhai *et al*. 2020, Wang *et al*. 2018, Kennedy *et al*. 2012). One alternative to control the accumulative plastic deformation is using the PRE technique to provide an additional confining stress for the embankment soil so as the σ_{cri} of the soil remains lager than the dynamic stress induced by the operation trains. The σ_{cri} is closely related to the confining pressure of the soil, and the correlation can be determined by performing dynamic triaxial tests under different confining pressures and dynamic deviator stresses (Zhai *et al*. 2020, Xiao *et al*. 2014, Dawson *et al*. 2000); the required σ_H of the embankment soil can therefore be determined.

The proposed analytical model is capable to calculate the σ_H at any point in a PRE subjected to multiple reinforcement devices/LPPs. Theoretically, a relationship between the LPP spacing and the pre-tension force of the steel reinforcement bars can be obtained with knowing the required σ_H. Fig. 16 illustrates a potential application of the analytical model, where the net spacing of the square LPPs along the longitudinal (L_1) and slope (L_2) directions and the pretension force F of the steel reinforcement bars can be adjusted to attain the required σ_H at a prescribed depth under the rail (i.e., the train wheel) by using the proposed analytical model, e.g., with knowing the L_1, L_2, and σ_H, the required F can be evaluated using the proposed analytical model. However, the detailed relationship among L_1, L_2, F, and σ_H needs further study in further.

7. Conclusions

An analytical model for the newly developed PRE is proposed to calculate the additional confining stress (σ_H) at any point in a PRE. For the aim of convenience in application, calculation charts were then developed in terms of three dimensionless parameters, and can be used to accurately and efficiently predict the σ_H in a PRE regardless of the embankment slope ratio and LPP side length ratio. The following conclusions can be drawn from this study.

(1) An analytical model was proposed to calculate the additional confining stress in the newly developed PRE; this model shows sufficient accuracy when the net spacing between the LPP and the line of embankment shoulder is greater than a certain value (e.g., two times of the LPP width (i.e., 2.0 m) in this study).

(2) The distribution of σ_H in the horizontal projection area of an LPP is changed from a "bulging abdomen" pattern to a relatively uniform "flat abdomen" pattern with increasing the horizontal distance (h) to the slope surface. The σ_H in the external regions of an LPP quickly increases to the peak, which is followed by a decrease with the increase in h. The horizontal distance from the peak stress point to the slope surface increases with increasing external distance, indicating that the σ_H is gradually spreads outward as h increases. Moreover, an effective reinforced zone can probably be formed in deep embankment soil.

(3) The trends of the coefficients of the additional confining stress (K_{HU} or K_{HD}) below the upper (or lower) corner points of an LPP versus h/w curves under different slope ratios are similar. The K_{HU} and its attenuation rate decrease with increasing h/w. The K_{HD} initially increases to the peak and then gradually decreases with increasing h/w when l/w is greater than $(l/w)_c$. Moreover, the side length ratio l/w of the LPP is suggested to be greater than the critical value $(l/w)_c$ but less than 4.0.

Acknowledgments

The research described in this paper was financially supported by the the National Natural Science Foundation of China (Grant No. 51978672, 51709284, and 51678572) and the Graduate Innovation Project of Central South University (Grant No. 2019zzts283).

References

Bi, J.F., Luo, X.Q., Zhang, H.T. and Shen, H. (2019), "Stability analysis of complex rock slopes reinforced with prestressed anchor cables and anti-shear cavities", *B. Eng. Geol. Environ*., **78**(3), 2027-2039. https://doi.org/10.1007/s10064-017-1171-8

Bobet, A. and Einstein, H.H. (2011), "Tunnel reinforcement with rockbolts", *Tunn. Undergr. Sp. Tech*., **26**, 100-123. https://doi.org/10.1016/j.tust.2010.06.006

Boussinesq, J. (1885), *Application des potentiels à l'étude de l'équilibre et du mouvement des solides élastiques*, Gauthier-Villars, Paris, France.

Budhu, M. (2011), *Soil Mechanics and Foundations*, John Wiley & Sons, New York, NY, USA.

Carranza-Torres, C. (2009), "Analytical and numerical study of the mechanics of rockbolt reinforcement around tunnels in rock masses", *Rock Mech. Rock Eng*., **42**, 175-228. https://doi.org/10.1007/s00603-009-0178-2

Castro-Fresno, D., Lopez, Q.L., Blanco-Fernandez, E. and Zamora-Barraza, D. (2009), "Design and evaluation of two laboratory tests for the nets of a flexible anchored slope stabilization system", *Geotech. Test. J*., **32**(4), 1-10.

Cerruti, V. (1882), *Ricerche intorno all'equilibrio de corpi elastici isotropi*, Atti della R. Accademia dei Lincei, Memoriae della classe di scienze fisiche, matematiche e naturali, Coi tipi del Salviucci, Roma, Italy.

Chen, R.P., Chen, J.M. and Wang, H.L. (2014), "Recent research on the track-subgrade of high-speed railways", *J. Zhejiang Univ.-Sc. A*, **15**(12), 1034-1038. https://doi.org/10.1631/jzus.A1400342

Das, A. and Bajpai, P.K. (2018), "A hypo-plastic approach for evaluating railway ballast degradation", *Acta Geotech*., **13**(5), 1085-1102. https://doi.org/10.1007/s11440-017-0584-7

Das, B. and Sobhan, K. (2014), *Principles of Geotechnical Engineering*, Cengage Learning, Boston, MA, USA.

Dawson, A., Mundy, M. and Huhtala, M. (2000), "European research into granular material for pavement bases and subbases", *Transport. Res. Rec.*, **1721**(1), 91-99. https://doi.org/10.3141/1721-11

Deng, D.P., Zhao, L.H. and Li, L. (2017), "Limit-equilibrium analysis on stability of a reinforced slope with a grid beam anchored by cables", *Int. J. Geomech.*, **17**(9), article no. 06017013. https://doi.org/10.1061/(ASCE)GM.1943-5622.0000964

Dong, J., Wu, Z.H., Li, X. and Chen, H.Y. (2018), "Dynamic response and pile-soil interaction of a heavy-haul railway embankment slope reinforced by micro-piles", *Comput. Geotech.*, **100**, 144-157. https://doi.org/10.1016/j.compgeo.2018.04.005

Esmaeili, M. and Arbabi, B. (2015), "Railway embankments stabilization by tied back-to-back system", *Comput. Geotech.*, **67**, 110-120. https://doi.org/10.1016/j.compgeo.2015.02.019

Esmaeili, M., Naderi, B., Neyestanaki, H.K. and Khodaverdian, A. (2018), "Investigating the effect of geogrid on stabilization of high railway embankments", *Soils Found.*, **58**(2), 319-332. https://doi.org/10.1016/j.sandf.2018.02.005

Fahimifar, A. and Ranjbarnia, M. (2009), "Analytical approach for the design of active grouted rockbolts in tunnel stability based on convergence-confinement method", *Tunn. Undergr. Sp. Tech.*, **24**, 363-375. https://doi.org/10.1016/j.tust.2008.10.005

German Railway Standard Rail 836 (2008), *Erdbauwerkeplanen, bauen und instandhalten*.

Gong, Q.M. and Zhou, S.H. (2007), *Railway Subgrade Engineering*, China Railway Publishing House, Beijing, China.

Guan, Z.C., Jiang, Y.J., Tanabasi, Y. and Huang, H.W. (2007), "Reinforcement mechanics of passive bolts in conventional tunneling", *Int. J. Rock Mech. Min. Sci.*, **44**, 625-636. https://doi.org/10.1016/j.ijrmms.2006.10.003

Guo, X.Q., Mao, X.B., Ma, C. and Huang, J.L. (2013), "Bolt support mechanism based on elastic theory", *Int. J. Min. Sci. Techno.*, **23**(4), 469-474. https://doi.org/10.1016/j.ijmst.2013.07.002

Kece, E., Reikalas, V., DeBold, R., Ho, C.L., Robertson, I. and Forde, M.C. (2019), "Evaluating ground vibrations induced by high-speed trains", *Transp. Geotech.*, **20**, article no.100236. https://doi.org/10.1016/j.trgeo.2019.03.004

Kennedy, J.H., Woodward, P.K., Banimahd, M. and Medero, G.M. (2012), "Railway track performance study using a new testing facility", *P. I. Civil Eng.-Geotec.*, **165**(5), 309-319. https://doi.org/10.1680/geng.10.00075

Khan, M.R. and Dasaka, S.M. (2019), "Quantification of ground-vibrations generated by high speed trains in ballasted railway tracks", *Transp. Geotech.*, **20**, article no. 100245. https://doi.org/10.1016/j.trgeo.2019.100245

Lazorenko, G., Kasprzhitskii, A., Khakiev, Z. and Yavna, V. (2019), "Dynamic behavior and stability of soil foundation in heavy haul railway tracks: A review", *Constr. Build. Mater.*, **205**, 111-136. https://doi.org/10.1016/j.conbuildmat.2019.01.184

Li, D.Q. (2018), "25 years of heavy axle load railway subgrade research at the facility for accelerated service testing (FAST)", *Transp. Geotech.*, **17**(part A), 51-60. https://doi.org/10.1016/j.trgeo.2018.09.003

Li, S.L., Wang, X., Liu, H.Z., Zhou, Y., Su, W. and Di, H. (2020), "Dynamic deflection monitoring of high-speed railway bridges with the optimal inclinometer sensor placement", *Smart Struct. Syst., Int. J.*, **26**(5), 591-603. https://doi.org/10.12989/sss.2020.26.5.591

Lv, W.T. and Wang, Y.H. (2004), "Dynamic stress analysis of subgrade-bridge transition section of Qin-Shen railway", *Chin. J. Rock Mech. Eng.*, **23**(3), 500-504.

Marjani, S.R. and Younesian, D. (2019), "Application of dithering control for the railway wheel squealing noise mitigation", *Smart Struct. Syst., Int. J.*, **23**(4), 347-357. https://doi.org/10.12989/sss.2019.23.4.347

Mei, H.H., Leng, W.M, Nie, R.S., Liu, W.J., Chen, C. and Wu, X.W. (2019), "Random distribution characteristics of peak dynamic stress on the subgrade surface of heavy-haul railways considering track irregularities", *Soil Dyn. Earthq. Eng.*, **116**, 205-214. https://doi.org/10.1016/j.soildyn.2018.10.013

National Railway Administration of the People's Republic of China (2014), *Code for design of high speed railway /TB 10621–2014*), China Railway Publishing House, Beijing, China.

Ozhan, H.O. and Guler, E. (2018), "Critical tendon bond length for prestressed ground anchors in pullout performance tests conducted in sand", *Int. J. Civ. Eng.*, **16**(10), 1329-1340. https://doi.org/10.1007/s40999-017-0261-0

Palop, K., Ivanović, A. and Brennan, A.J. (2013), "Centrifuge modeling of the nondestructive testing of soil anchorages", *J. Geotech. Geoenviron.*, **139**(6), 880-891. https://doi.org/10.1061/(ASCE)GT.1943-5606.0000788

Papanastassopoulou-Tsatsanifou, F. (1983), "Investigation of effect of rock bolts on stress distribution around underground excavations", *Proceedings of the International Symposium on Rock Bolting*, Abisko, Sweden, August–September.

Roghani, A., Macciotta, R. and Hendry, M.T. (2017), "Quantifying the effectiveness of methods used to improve railway track performance over soft subgrades: Methodology and case study", *J. Transp. Eng. A-Syst.*, **143**(9), article no. 04017043. https://doi.org/10.1061/JTEPBS.0000071

Sayeed, M.A. and Shahin, M.A. (2018), "Design of ballasted railway track foundations using numerical modelling. Part I: Development", *Can. Geotech. J.*, **55**(3), 353-368. https://doi.org/10.1139/cgj-2016-0633

Shi, K.Y., Wu, X.P., Liu, Z. and Dai, S.L. (2019), "Coupled calculation model for anchoring force loss in a slope reinforced by a frame beam and anchor cables", *Eng. Geol.*, **260**, article no. 105245. https://doi.org/10.1016/j.enggeo.2019.105245

Showkati, A., Maarefvand, P. and Hassani, H. (2015), "Stresses induced by post-tensioned anchor in jointed rock mass", *J. Cent. South Univ.*, **22**(4), 1463-1476. https://doi.org/10.1007/s11771-015-2664-x

Showkati, A., Maarefvand, P. and Hassani, H. (2016), "An analytical solution for stresses induced by a post-tensioned anchor in rocks containing two perpendicular joint sets", *Acta Geotech.*, **11**(2), 415-432. https://doi.org/10.1007/s11440-015-0371-2

Skrypnyk, R., Nielsen, J.C.O., Ekh, M. and Pålsson, B.A. (2019), "Metamodelling of wheel–rail normal contact in railway crossings with elasto-plastic material behaviour", *Eng. Comput.*, **35**(1), 139-155. https://doi.org/10.1007/s00366-018-0589-3

Sun, Q., Indraratna, B. and Ngo, N.T. (2019), "Effect of increase in load and frequency on the resilience of railway ballast", *Géotechnique*, **69**(9), 833-840. https://doi.org/10.1680/jgeot.17.P.302

Tang, L., Yan, M.H., Ling, X.Z. and Tian, S. (2016), "Dynamic behaviours of railway's base course materials subjected to long-term low-level cyclic loading: experimental study and empirical model", *Géotechnique*, **67**(6), 537-545. https://doi.org/10.1680/jgeot.16.P.152

Terzaghi, K., Peck, R.B. and Mesri, G. (1996), *Soil Mechanics in Engineering Practice*, John Wiley & Sons, New York, NY, USA.

Wang, Y.X. (2019), "Study on model test system of a new prestressed subgrade and analysis of the additional stress field", Master Dissertation; Central South University, Changsha, China.

Wang, J., Liu, S. and Yang, W.B. (2018), "Dynamics shakedown analysis of slab track substructures with reference to critical

speed", *Soil Dyn. Earthq. Eng.*, **106**, 1-13. https://doi.org/10.1016/j.soildyn.2017.12.004

Wang, H., Zhu, Q.X., Li, J., Mao, J.X., Hu, S.T. and Zhao, X.X. (2019), "Identification of moving train loads on railway bridge based on strain monitoring", *Smart Struct. Syst., Int. J.*, **23**(3), 263-278. https://doi.org/10.12989/sss.2019.23.3.263

Wang, K., Cao, W.X., Su, Z.Q., Wang, P.X., Zhang, X.J., Chen, L.J., Guan, R.Q. and Lu, Y. (2020), "Structural health monitoring of high-speed railway tracks using diffuse ultrasonic wave-based condition contrast: theory and validation", *Smart Struct. Syst., Int. J.*, **26**(2), 227-239. https://doi.org/10.12989/sss.2020.26.2.227

Wu, Y., Mao, X.B., Huang, J.L., Sun, F.J. and Yao, B.H. (2010), "Action mechanism of a mechanical end-anchorage bolt", *Int. J. Min. Sci. Technol.*, **20**(4), 625-628. https://doi.org/10.1016/S1674-5264(09)60256-8

Wu, Q.H., Li, X.B., Weng, L., Li, Q.F., Zhu, Y.J. and Luo, R. (2019), "Experimental investigation of the dynamic response of prestressed rockbolt by using an SHPB-based rockbolt test system", *Tunn. Undergr. Sp. Tech.*, **93**, article no. 103088. https://doi.org/10.1016/j.tust.2019.103088

Xiao, J.H., Juang, C.H., Xu, C.J., Li, X.W. and Wang, L. (2014), "Strength and deformation characteristics of compacted silt from the lower reaches of the Yellow River of China under monotonic and repeated loading", *Eng. Geol.*, **178**, 49-57. https://doi.org/10.1016/j.enggeo.2014.06.008

Xu, F., Leng, W.M., Nie, R.S., Zhang, Q.S. and Yang, Q. (2018a), "New structure for strengthening soil embankments", *Adv. Civ. Eng.*, **2018**, article no. 4809034. https://doi.org/10.1155/2018/4809034

Xu, F., Yang, Q., Liu, W.J., Leng, W.M., Nie, R.S. and Mei, H.H. (2018b), "Dynamic stress of subgrade bed layers subjected to train vehicles with large axle loads", *Shock Vib.*, **2018**, article no. 2916096. https://doi.org/10.1155/2018/2916096

Xu, F., Zhai, B., Leng, W.M., Yang, Q., Leng, H.K. and Nie, R.S. (2020), "Probabilistic method for evaluating the permanent strain of unbound granular materials under cyclic traffic loading", *Constr. Build. Mater.*, **251**, article no. 118975. https://doi.org/10.1016/j.conbuildmat.2020.118975

Zhai, B., Leng, W.M., Xu, F., Zhang, S., Ye, X.Y. and Leng, H.K. (2020), "Critical dynamic stress and shakedown limit criterion of coarse-grained subgrade soil", *Transp. Geotech.*, **23**, article no. 100354. https://doi.org/10.1016/j.trgeo.2020.100354

CC